LANGMUIR

Article

pubs.acs.org/Langmuir

Formation of Small Gold Nanoparticle Chains with High NIR Extinction through Bridging with Calcium Ions

Robert J. Stover,[†] Ehsan Moaseri,[‡] Sai P. Gourisankar,[‡] Muhammad Iqbal,[‡] Negin K. Rahbar,[§] Behzad Changalvaie,[‡] Thomas M. Truskett,[†,‡] and Keith P. Johnston*[,†,‡]

[†]Texas Materials Institute, [‡]McKetta Department of Chemical Engineering, and [§]Department of Chemistry, University of Texas at Austin, Austin, Texas 78712, United States

Supporting Information

ABSTRACT: The self-assembly of citrate-capped Au nanoparticles (5 nm) resulted in branched nanochains by adding $CaCl_2$ versus spherical nanoclusters for NaCl. These assemblies were formed between 1 s to 30 min by tuning the electrostatic repulsion and the interparticle bridging attraction between the cations and citrate ligands as a function of electrolyte concentration. For dilute Ca^{2+}, strong interparticle bridging favored particle attachment at chain ends. This resulted in the formation of small, branched chains with lengths as short as 20 nm, due to the large Debye length for the diffuse counterions. Furthermore, the bridging produced very small interparticle spacings and sintering, as evident in high-resolution TEM despite the low temperature. This morphology produced a large red shift in the surface plasmon resonance, as characterized by a broad extinction peak with NIR absorption out to 1000 nm, which is unusual for such small particles. Whereas these properties were seen for primary particles with partial citrate monolayers, the degrees of sintering and NIR extinction were small in the case of citrate multilayers. The ability to design the size and shape of nanoparticle clusters as well as the interparticle spacing by tuning bridging and electrostatic interactions may be expected to be quite general and of broad applicability in materials synthesis.

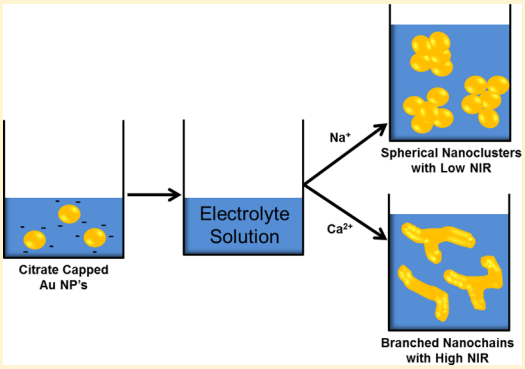

INTRODUCTION

Nanoparticle clusters (nanoclusters, supraparticles) may be assembled from primary metal and semiconductor nanospheres by tuning the colloidal interactions. The morphology may be controlled from 1D chains to 3D spherical aggregates by an emerging understanding of how to balance the interparticle electrostatic and steric repulsion against the van der Waals (vdW) attraction, dipolar interactions, hydrophobic interactions, hydrogen bonding between ligands on the surface, and bridging interactions of these ligands with ions.[1−5] "Pearl necklace" aggregates of closely spaced CdTe primary particles have been formed upon removal of thioglycolic acid (TGA) ligands from the surface to decrease electrostatic repulsion.[6] In this case, the permanent dipoles on the semiconductor nanocrystals provided an anisotropic force to guide linear assembly as has been described by Monte Carlo computer simulation.[7] For citrate-stabilized Au nanoparticles (NPs), the formation of large dipoles on the NPs, upon partial replacement of citrate with 2-mercaptoethanol, was utilized to synthesize long branched chains.[8] Zhang and Wang presented a model for the formation of 1D chains based on a stronger net electric field and thus greater electrostatic repulsion of a particle at the side of a chain relative to the chain end.[9] The chain length could be controlled by varying the electrostatic repulsion relative to the vdW attraction and dipolar interactions arising from the surface ligands. Enustun and Turkevich hypothesized that 1-D chains may be formed under slow coagulation (days to months) with a small surface charge and at low ionic strength where the diffuse counterion layer is thick.[10] As expected from this concept, long branched chains composed of 10 nm citrate-coated Au NPs in ethanol/water mixtures were formed by adding less than 1 mM NaCl to reduce the electrostatic repulsion.[11]

One of the simplest methods used to investigate the mechanism and rate of NP assembly is to control the electrostatic repulsion with inorganic electrolytes to vary the Debye length, as described by DLVO theory.[10,12−14] For Au NPs with carboxylate ligands, the rate of aggregation is influenced strongly by the bridging attraction between the ligands upon addition of monovalent cations.[13,15,16] These bridging interactions become much stronger for divalent ions.[12,17] For example, Ca^{2+}, Cu^{2+}, and Fe^{2+} have been used to chelate Ag and Au particles stabilized by lipoic acid in order to form multilayer 3D close-packed structures.[18] Au NPs were also assembled into monodisperse spherical clusters (>100 nm) by bridging carboxylate anions with Zn^{2+} and Cd^{2+} with close-packed order.[16] If this bridging attraction could be properly modulated against electrostatic repulsion and vdW attraction,

Received: September 29, 2015
Revised: January 5, 2016
Published: January 6, 2016

DOI: 10.1021/acs.langmuir.5b03639
Langmuir 2016, 32, 1127−1138

then it might be possible to control the morphology and spectral and electronic properties of 1D nanoclusters as well as 3D nanoclusters.

To date, relatively few studies have reported the colloidal assembly of Au and Ag nanoclusters smaller than 70 nm from presynthesized sub-10-nm primary particles. These small clusters are of great interest in many applications including biomedical imaging and therapy,[19,20] sensors,[4] catalysis,[21] and conductors for electronics.[22] In the field of biomedical imaging and therapy, NPs smaller than 70 nm are often favored because they have slower uptake by the reticuloendothelial system (RES) and also undergo more rapid endocytosis in cancer cells.[23]

For nanoclusters with very closely spaced primary particles, the extinction spectra of the surface plasmon resonance (SPR) shift into the NIR region from 700 to 1100 nm, where blood and tissue are relatively transparent.[4,20,24,25] The red shift increases as the spacing between the primary particles decreases and the number of particles within a cluster (aggregation number) increases because these factors influence the instantaneous dipoles and multipoles of the oscillating electrons.[26−30] To shift the SPR to 1000 nm, the edge-to-edge spacing should be $\lesssim$5% of the particle diameter.[31] For example, Au NPs stabilized by a very short ligand, homocysteine, exhibit SPR band shifts to 800 nm for aggregates of 30 nm Au particles but only to 650 nm for 11 nm particles.[32] Thus, it appears to be a major challenge to shift the SPR to 1000 nm for sub-10-nm NPs.

A potential strategy for assembling Au nanoclusters with high NIR extinction would be to design an incomplete, nonuniform coverage of ligands on the particle surfaces to allow very close interparticle spacing on the order of <0.5 nm. Limited surface coverage has been used to achieve such small spacings for "pearl necklaces" whereby they could be further converted to nanowires.[6] Similarly, 14 nm citrate-capped gold NPs adsorbed at an oil-in-water interface underwent coalescence (sintering) to form wires over 7 days, resulting in a red shift in the NIR extinction to 1000 nm.[33] Furthermore, small Au nanoclusters with close spacings and strong NIR extinction were produced by exchanging citrate ligands with very weakly bound lysine molecules to weaken electrostatic repulsion.[34] For citrate ligands on Au NPs, an edge-to-edge spacing of 1.28 nm has been observed, which is slightly smaller than twice the estimated thickness of 0.7 to 1 nm for a citrate layer on Au.[35] Given that broad NIR extinction out to 1100 nm was observed for ~70 nm Au nanoclusters composed of very small 5 nm primary particles coated with citrate ligands, the spacing between primary particles was likely less than 1.28 nm.[36−39] Moderate NIR extinction at 1000 nm was observed for 5 nm citrate-capped gold NPs assembled into mostly linear aggregates after covalent modification with *N*-ethyl-*N*-(dimethylaminopropyl)carbodiimide (EDC).[36] However, high-resolution TEM (HR-TEM) images indicated that the 70−100 nm aggregates underwent partial sintering from Ostwald ripening. In a related study, sintering between closely spaced NPs led to strong NIR shifts upon removal of citrate stabilizers from gold NP surfaces, although the aggregate size was not controlled.[40] Furthermore, at room temperature, 10 nm citrate-capped Ag particles have been shown to undergo coalescence upon close contact after solvent evaporation.[41] On the basis of these advances, a remaining challenge would be to utilize interparticle attractive interactions with incomplete ligand coverage on the surface to achieve very closely spaced primary particles to achieve strong NIR extinction for small nanoclusters with controlled shape.

Herein, we tune the assembly of 5 nm citrate-capped Au primary nanospheres to form either 1D or 3D nanostructures simply by adding monovalent or divalent cations to manipulate the colloidal interactions. Our hypothesis is that the utilization of a bridging attraction between cations and the citrate ligands, in addition to vdW and dipolar attraction, offers an additional degree of freedom to gain greater control over the cluster size, shape, and interparticle spacing. The electrostatic repulsion and the interparticle bridging attraction are varied simply by changing the concentration of either Na^+ or Ca^{2+} at pH 7. A mechanism is presented in Figure 1 to describe the change

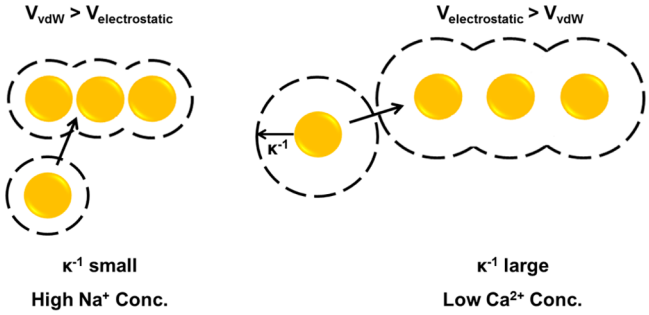

Figure 1. Schematic of the assembly of gold NPs into spherical and linear chain morphologies. With short Debye lengths at high Na^+ concentrations, a greater influence of the vdW potential versus electrostatic repulsion causes an addition to the cluster in nonselective locations. For low Ca^{2+} concentrations, the stronger electrostatic repulsion with long Debye length particles results in the selective addition of NPs to the chain ends.

from 3D nanoclusters observed with Na^+ to branched nanochains with Ca^{2+} by varying the range and strength of the electrostatic interactions relative to the bridging interaction. To form nanochains, thick diffuse counterion layers were used at low Ca^{2+} concentrations to achieve selective nanocluster growth on the chain ends relative to the sides, in the presence of the strong short-ranged bridging interaction. The effect of cation charge and concentration on the spacing between the primary particles within the nanocluster is evaluated from TEM micrographs and the red shift in the SPR. Sintering of the primary particles was observed for Ca^{2+} as a consequence of small interparticle spacings resulting from the strong interparticle bridging attraction. During the approach of the NPs, the diffusion of citrate molecules along the surface or citrate desorption[11] may allow for close interparticle spacings in the clusters, given that Park et al. reported citrate coverages of only ~45% on gold NP surfaces.[35] We demonstrate that close spacings and sintering may be used to achieve strong NIR extinction out to 1100 nm in short nanochains with lengths from 20 to 50 nm. To harvest the growing nanoparticle clusters at short times, they were quenched simply by dilution to lower the ion concentration and were found to be stable for 20 days.

METHODS AND MATERIALS

Tetrachloroauric acid ($HAuCl_4 \cdot 3H_2O$) was purchased from Acros Chemicals (Morris Plains, NJ). Sodium borohydride ($NaBH_4$), sodium citrate ($Na_3C_6H_5O_7 \cdot 2H_2O$), calcium chloride ($CaCl_2$), and sodium chloride (NaCl) were obtained from Fisher Chemical (Fair Lawn, NJ).

Synthesis of Primary Citrate-Capped Nanospheres and Addition or Removal of Citrate. Citrate-capped ~4 nm primary nanospheres were synthesized via a previously reported procedure.[37,42]

DOI: 10.1021/acs.langmuir.5b03639
Langmuir 2016, 32, 1127−1138

First, 30 mL of a 25.4 mM $HAuCl_4 \cdot 3H_2O$ solution was added to 3 L of DI water at 95 °C under vigorous stirring. Next, 30 mL of a 34.0 mM $Na_3C_6H_5O_7 \cdot 2H_2O$ solution was added to the boiling solution to initiate the reduction of the gold ions. Approximately 1 min later as the solution darkened, an additional 30 mL of 34.0 mM $Na_3C_6H_5O_7 \cdot 2H_2O$ was added to aid particle stabilization along with 19.8 mM $NaBH_4$ for complete Au^{3+} reduction, resulting in a bright red color. The solution was then cooled in an ice bath before centrifugation at 14 000 rcf for 10 min to remove large aggregates. To achieve a final Au solution concentration of 3 mg/mL, the supernatant was then concentrated using tangential flow filtration (TFF) with a 10 kDa PES filter to a final volume of ∼200 mL, followed by centrifugation of 15 mL batches with 30 kDa PES Millipore filter centrifuge tubes at 6000 rpm for 5 min. The retentates were combined to give a final solution volume of ∼10 mL. Finally, approximately 20 mL of DI water (pH 6.90) was added to the retentate to achieve a final Au concentration of ∼3 mg/mL and a final sodium citrate concentration of 0.3 mM. The pH of the solution was 6.60.

To decrease the number of excess citrate ions in the solution and on the Au surfaces for only one particular set of experiments, 2 mL of a 3 mg/mL Au solution was diluted with 5 mL of DI water, placed into a 30 kDa filter centrifuge tube, and spun at 6000 rpm for 5 min to a final volume of ∼0.5 mL. Once finished, an additional 6.5 mL of fresh DI water was added, and the sample was centrifuged a second time. This procedure was repeated two more times. This low citrate sample was then diluted to 0.3 mg/mL Au with DI water with a pH value of 6.98 for nanocluster formation.

Under some circumstances, a 100/1 molar excess of sodium citrate was added to the as-prepared gold nanoparticles at 0.3 mg/mL Au. In this case, the concentration of sodium citrate in the system was increased from ∼0.03 to 3 mM. However, the excess sodium citrate was added directly to the reaction mixture containing DI and electrolytes during cluster formation. No prior incubation of the particles with the excess sodium citrate took place prior to cluster formation.

Characterization of Nanospheres. Nanospheres were diluted to ∼0.3 mg/mL Au and filtered through a 200 nm poly(ether sulfone) (PES) syringe filter prior to dynamic light scattering (DLS), zeta potential, and UV−vis−NIR measurements. As reported previously,[37,38] hydrodynamic size distributions were measured on a Brookhaven ZetaPALS instrument using a 90° detection angle using a non-negatively constrained least-squares multiple pass (NNLS) method and an autofit slope analysis option. Sizes of less than 3 nm were ignored in the reported distributions on the basis of TEM micrographs, which indicated no particles below that size (Figure S1; Table S6, row 16). Also it is well known that DLS models may yield unphysically small peaks for gold particles.[43] Intensity-weighted DLS distributions are given for several samples in the Supporting Information. For systems with small absorbance at the laser wavelength (650 nm), we also report volume distributions. For systems with high absorption at 650 nm, the conversion from the intensity distribution to the volume distribution would require Mie theory analysis, which is beyond the scope of this study. Thus, for systems with an absorbance ratio, $A_{1000/525}$, greater than 0.1, we report the minimum value of the larger NNLS intensity-weighted peak. The larger peaks were ignored because very small fractions of large particles create intense scattering. This protocol was found to yield diameters that were in agreement with the TEM number-average diameters as shown in Table S7.

The zeta potentials were measured using the Brookhaven ZetaPALS instrument in ZetaPALS mode. The gold concentration of the measured samples was 0.015 mg/mL at pH 7 and at various ionic strengths of NaCl and $CaCl_2$. Here the concentration was very dilute to minimize particle aggregation prior to measurement. A minimum of 5 runs were performed for each sample with 10 cycles with an average applied electric field of ∼9 V/cm. All values reported assume the Hückel model. UV−vis−NIR spectroscopy was obtained with a Varian Cary 60 spectrophotometer with a sample path length of 1 cm. Extinction peaks were normalized to 1 for clarity of comparison. Most extinction results are reported as ratios of the absorbance at 1000 nm relative to 525 nm, termed $A_{1000/525}$, throughout this study.

Thermogravimetric analysis (TGA) measurements were made with a Mettler Toledo TGA/DSC 1 STAR. Samples were dried under desiccated air. The final sample was heated from 25 to 900 °C at a rate of 10 °C/min under nitrogen flow.

Gold concentrations were determined through flame atomic absorption spectroscopy (FAAS) using a GBC 908AA analyzer (GBC Scientific Equipment Pty Ltd.) with an air/acetylene flame at a wavelength of 242.8 nm. Samples were prepared by dissolving a known volume of nanospheres in an aqua regia (3:1 HCl/HNO_3 v/v) solution before exposing them to a flame. The absorbance data were then related to a set of Au standards of known mass to determine the sample concentration.

Nanocluster Formation. Varying amounts of 5% NaCl or 0.5% $CaCl_2$ were added to DI water prior to Au NP addition for a final volume of 1 mL. Then, 1 mL of the 0.3 mg/mL citrate nanoparticle solution was added to a final Au concentration of 0.15 mg/mL. The electrolyte concentrations reported throughout the paper are the concentrations after both solutions are mixed. At differing time points, 200 μL of the resulting solution was removed and diluted to 0.025 mg/mL Au in 1 mL of DI water to reduce the concentration of electrolyte and Au to effectively quench the reaction by increasing the electrostatic repulsion and reducing the rate of interparticle collisions.

Nanocluster Characterization. Immediately after cluster dilution, nanocluster samples underwent DLS and UV−vis−NIR measurements. Certain samples also underwent zeta potential and TEM analysis after both DLS and UV−vis−NIR were complete. Given that the samples were already dilute, only samples for TEM were diluted further to a final concentration of ∼5×10^{-4} mg/mL Au prior to measurement. TEM samples were prepared by placing a 5 μL drop of a given sample onto a 200-mesh carbon type-A grid (Ted Pella, Redding, CA). The majority of the drop was then wicked off using a Kimwipe to form a thin liquid film on the grid that was then immersed in liquid nitrogen and lyophilized overnight at −40 °C using a VirTis AdVantage tray lyophilizer (VirTis, Gardiner, NY). The samples were then examined using an FEI TECNAI G2 F20 X-TWIN TEM with a high-angle annular dark-field detector with an accelerating voltage of 80 kV.

RESULTS AND DISCUSSION

Characterization of Primary Citrate-Coated Au Nanospheres. For the citrate-capped gold NPs synthesized by the reduction of $HAuCl_4$ with $NaBH_4$[44] (labeled "as prepared" in Table 1), UV−vis−NIR extinction, TEM core diameters, and zeta potential measurements agreed closely with those in previous studies (Table 1).[37,45] Additionally, the polydispersity (± std deviation), 5.0 ± 0.7 nm, was low for the TEM number-average distribution measured from sizing 100 NPs (Figure S1; Table S6, row 16). A small number of dimers and trimers were observed, likely as a result of attractive capillary forces during the drying step of grid preparation. Similar measured sizes and behavior were observed for particles incubated in 3 mM sodium citrate, which is an excess of 100× compared to the as-prepared citrate particles that contained ∼0.03 mM total sodium citrate

Table 1. Characteristics of Primary Au Particles with Various Citrate Concentrations

	as prepared	100× citrate	low citrate
$A_{1000/525}$	0.02	0.01	0.03
TEM volume avg (nm)	5.0 ± 0.7	5.0 ± 1.4	6.5 ± 1.9
zeta potential (mV)	−45.3 ± 1.7	−53.0 ± 3.5	−34.4 ± 2.2
organic content (wt %)	4.8 ± 0.3	not measured	3.3 ± 0.2

DOI: 10.1021/acs.langmuir.5b03639
Langmuir 2016, 32, 1127−1138

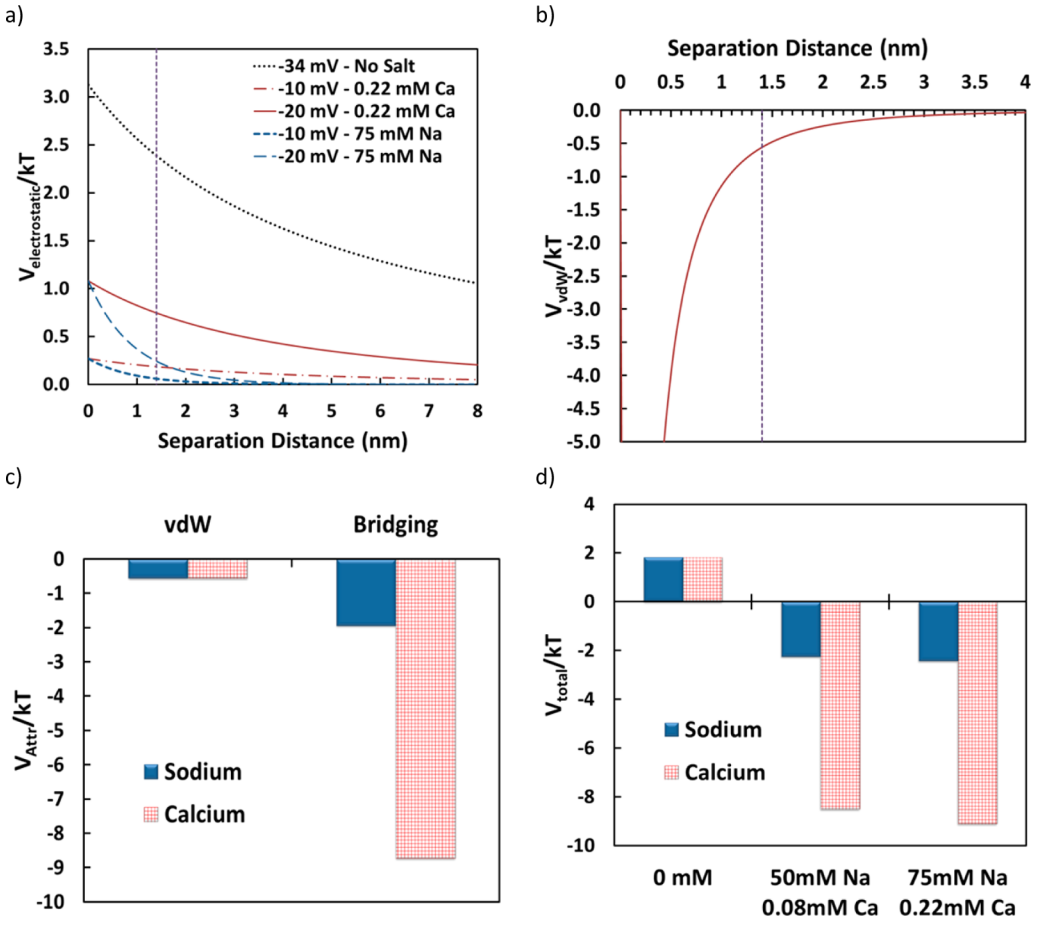

Figure 2. (a) Electrostatic potential for 5 nm primary citrate particles for various surface potentials and varying NaCl and $CaCl_2$ concentrations. (b) van der Waals potential for 5 nm primary particles. vdW and bridging attraction potentials (c) and total interaction potential (d) versus NaCl and $CaCl_2$ concentrations for a separation distance of 1.4 nm. The separation distance for two particles coated with citrate ligands is ~1.4 nm.

in the solution. For the 100× citrate particles, ζ decreased from −45.3 mV with a standard deviation of ±1.7 mV to −53.0 ± 3.5 mV, indicating additional citrate binding directly to the Au surface or H bonding to other citrate moieties through dangling carboxylates.[35] For a third "low-citrate" type of particle, which was produced by washing the as-prepared particles three times with DI water via filter centrifugation, ζ decreased in magnitude to −34.4 ± 2.2 mV and the organic content according to TGA dropped to 3.3 wt %. This decrease in stabilizing ligand led to moderate aggregation of the initial primary particles to 6.5 ± 1.9 nm via TEM analysis given a small population of dimers (Figure S1c), yet the size remained stable for weeks at room temperature.

Interaction Potentials for Mono- and Divalent Electrolytes. To provide a basis for describing the colloidal assembly, we begin by examining the total interaction potential V_{tot}, which is a sum of the vdW, bridging, and electrostatic potentials, all shown in Figure 2.[14] To understand the role of these particular terms, we did not include the unknown dipolar attraction and steric repulsion. The vdW potential can be expressed as

$$V_{vdW} = -\frac{A}{6}\left[\frac{2a^2}{H(4a+H)} + \frac{2a^2}{(2a+H)^2} + \ln\left(\frac{H(4a+H)}{(2a+H)^2}\right)\right] \quad (1)$$

where A is the Hamaker constant, H is the surface-to-surface separation distance, and a is the particle radius. The electrostatic potential may be expressed for symmetric and asymmetric electrolytes for surface potentials Ψ_0 < 25 mV as[14,46]

$$V_{electrostatic} = 4\pi\varepsilon_r\varepsilon_0 a^2\Psi_0^2 \exp\frac{-\kappa H}{H+2a} \quad (2)$$

where ε_r is the relative dielectric of the solvent, ε_0 is the dielectric constant in vacuum, and κ is the inverse Debye length given by

$$\kappa = \sqrt{\frac{1000e^2N_{A^*}}{\varepsilon_r\varepsilon_0 k_b T}}(2I)^{1/2} \quad (3)$$

where N_A is Avogadro's number and I is the ionic strength. Previous studies have shown mono- and divalent cations undergo bridging attraction with citrate ligands on Au NP surfaces, which may be treated as linearly proportional to the free energy of cation dissociation[15−17] as follows

DOI: 10.1021/acs.langmuir.5b03639
Langmuir 2016, 32, 1127−1138

Table 2. Debye Length and Primary Particle Zeta Potential (0.015 mg/mL Au) and Properties of the Clusters Formed 30 and 300 s after Electrolyte Addition to 0.15 mg/mL Au at pH 7 for Two Types of Primary Particles

				t_1 = 30 s			t_2 = 300 s		
primary particle	salt conc (mM)	κ^{-1} (nm)	primary Au ζ (mV)	D_H (nm)	$A_{1000/525}$	cluster ζ (mV)	D_H (nm)	$A_{1000/525}$	cluster ζ (mV)
−34 mV	0.08 $CaCl_2$	17.32	−20.9 ± 3.3	7.2	0.02	−19.6 ± 1.1	9.9	0.06	−30.7 ± 1.9
	0.22 $CaCl_2$	11.34	−16.4 ± 1.5	22.4	1.00	−31.8 ± 1.8	48.2	1.15	−26.8 ± 2.9
	50 NaCl	1.37	−24.0 ± 6.1	16.4	0.02	−36.0 ± 3.1	465	0.37	−46.9 ± 0.8
	75 NaCl	1.12	−16.8 ± 5.8	369	1.00	−27.6 ± 1.8	aggr	aggr	aggr
−45 mV	0.08 $CaCl_2$	17.32	−29.6 ± 0.9	7.7	0.03	−29.0 ± 1.6	15.6	0.10	−33.2 ± 1.5
	0.22 $CaCl_2$	11.34	−23.0 ± 1.8	25.0	0.60	−31.8 ± 1.3	49.5	0.84	−23.9 ± 4.0
	50 NaCl	1.37	−29.9 ± 2.1	26	0.01	−40.4 ± 1.9	180	0.28	−43.4 ± 0.6
	75 NaCl	1.12	−21.1 ± 0.8	243	0.82	−36.0 ± 2.9	Aggr	Aggr	Aggr

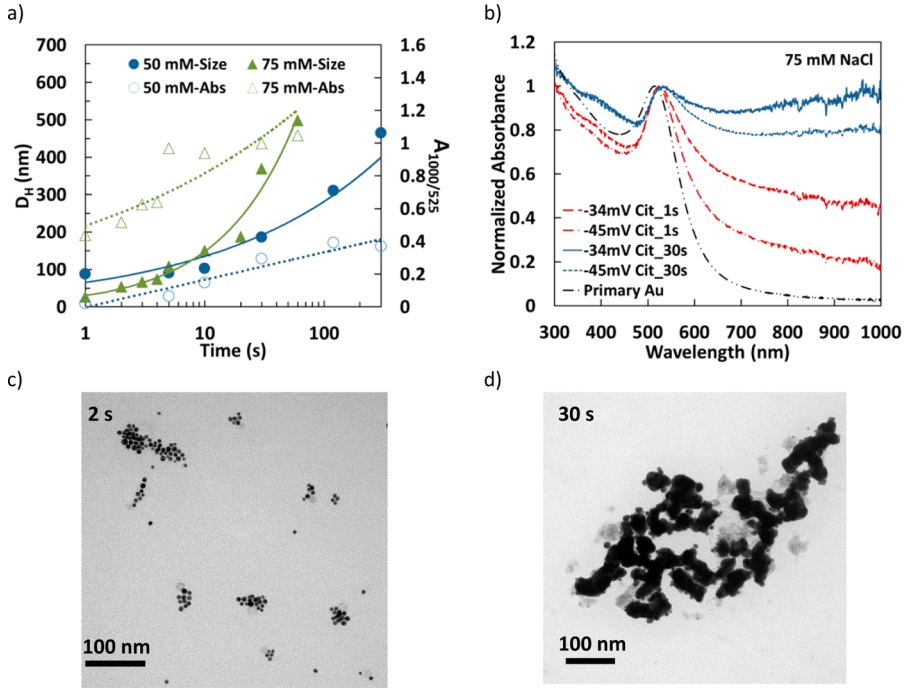

Figure 3. (a) Nanocluster D_H (DLS) and $A_{1000/525}$ ratio vs time for −34 mV primary particles for 50 and 75 mM NaCl. UV−vis−NIR extinction curves are shown in (b) for 75 mM NaCl for reaction times of 1 and 30 s. TEM image of clusters made with 75 mM NaCl after (c) 2 and (d) 30 s.

$$V_{bridging} = -f\Delta G_d \quad (4)$$

where f is a proportionality constant, taken to be 1.2, as established for monovalent cations with citrate by Wang et al.[15] The dissociation energy, ΔG_d for a cation from a citrate ligand is related to the equilibrium dissociation constant, K_d, through

$$\Delta G_d = -RT \ln(K_d) \quad (5)$$

The electrostatic energy is shown for the −34 mV particles at a low ionic strength of 0.22 mM for $CaCl_2$ and 75 mM for NaCl, whereby the surface potential was approximated by ζ. For the widely used electrolyte concentrations used in this paper, the surface potentials were chosen as −10 and −20 mV to reflect ζ values in Table 2 and the unknown cation adsorption in the Stern layer. Furthermore, V_{elec}/kT is stronger and much longer ranged for Ca^{2+} versus Na^+ as a consequence of the 114-fold lower I and consequently much longer κ^{-1} as shown in Table 2. It is instructive to examine the various contributions to V_{tot} at a separation distance of closest approach between two fully citrate-capped NPs of 1.4 nm. This distance is based on the measured 0.7 nm length of a citrate molecule on a gold surface.[35] Although V_{elec}/kT of the −34 mV particles is 2.4 without added electrolyte, it drops to below 1 in the presence of NaCl and $CaCl_2$ because of the lower surface potential (ζ) and increased ionic strength.

The attractive interaction energy between the particles is the sum of the vdW and bridging interaction potentials. The dissociation constants for Na^+- and Ca^{2+}-citrate complexes have been measured as 0.2 and 0.0007 M, respectively, indicating a significantly stronger binding affinity for a divalent cation.[47] The corresponding ΔG_d values were 6.6×10^{-21} and 3.0×10^{-20} J. As shown in Figure 1b, V_b was ∼4.5 times higher for Ca^{2+} than for Na^+, which will be shown below to have a large effect on the aggregation behavior. For the closest distance between two fully citrate-capped gold NPs of 1.4 nm, the vdW attraction is much smaller than the bridging interaction for both Na^+ and Ca^{2+}. Thus, the bridging attraction plays a dominant role in the total interaction potential, as further discussed below.

Effect of $CaCl_2$ and NaCl on the Debye Length and Zeta Potential of the Primary Particles. Before describing the particle aggregation to form the Au nanoclusters, we first examine the effect of each electrolyte on ζ at a very low Au concentration of 0.015 mg/mL where aggregation is minimal.

DOI: 10.1021/acs.langmuir.5b03639
Langmuir 2016, 32, 1127−1138

Both the as-prepared (−45 mV) and low citrate (−35 mV) particles were characterized for key electrolyte concentrations used throughout this study (Table 1). These concentrations were based on known critical coagulation concentrations (CCC) of citrate-capped metal NPs of ∼50−100 mM for NaCl and ∼2.1−2.5 mM for $CaCl_2$.[17,48] For dilute 0.08 and 0.22 mM $CaCl_2$, the Debye lengths were very large, 17.3 and 11.3 nm, respectively. For the much larger NaCl concentrations of 50 and 75 mM, the Debye lengths were much smaller, only 1.37 and 1.12 nm, respectively, as a consequence of the much larger ionic strengths.

The ζ values of the as-prepared and −34 mV primary particles dropped significantly with the added electrolytes in Table 2. With only 0.08 mM $CaCl_2$, ζ was −20.9 ± 3.3 and −29.6 ± 0.9 mV for −34 and −45 mV particles, respectively. For 0.22 Ca^{2+}, ζ dropped to −16.4 ± 1.5 and −23.0 ± 1.8 mV, indicating greater Debye screening and greater adsorption in the Stern layer. For NaCl as seen for $CaCl_2$, more negative ζ values were observed for the as-prepared −45 mV particles at the lower NaCl concentration.

Effect of NaCl on NP Aggregation. To further establish electrolyte concentrations for nanocluster formation, we first identified the critical coagulation concentration (CCC) at the diffusion-controlled limit. Here, the Smoluchowski half-life is 1.6 ms for 5 nm spheres at a concentration of 0.3 mg/mL Au. Immediate aggregation was observed visually for our system at ∼100 mM NaCl as the colloids grew to 75 nm within the shortest time measured, 1 s, and precipitated within 3 s (Figure S2). This concentration was essentially the CCC where the stability ratio became unity, given the loss of electrostatic repulsion and gain in bridging attraction. This value for a 5 nm particle is consistent with the trend in previously reported values of 48 mM for 60 nm and 122 mM for 30 nm Ag spheres.[17,48]

The nanoclusters in this study were formed at a gold concentration of 0.15 mg/mL with NaCl concentrations from 25 to 100 mM. For the lowest NaCl concentration, the hydrodynamic diameters, D_H, grew to only 15 and 18 nm over 1800 s, for −45 mV and −34 mV citrate particles, respectively (Table S2). The small aggregation was not enough to create any significant changes in the SPR for either sample as the $A_{1000/525}$ ratios remained <0.1. Notable size increases were observed as the concentration was doubled to 50 mM as shown for the −34 mV primary particles in Figure 3a. The NP cluster sizes grew to over 100 nm within 30 s and continued to increase steadily up to 300 s. Here, the $A_{1000/525}$ values increased moderately to ∼0.4 for the 465 nm aggregates, with the color of the solution becoming reddish purple (Table S4). A much higher NIR absorbance was observed for 75 mM NaCl as shown in the spectra at 1 and 30 s in Figure 3b for the −34 mV primary particle systems. With an NP cluster size of 50 nm, $A_{1000/525}$ reached ∼0.6 within 2 s. At 10 s, $A_{1000/525}$ rose to over 1.0, with a notable color change to purple as D_H grew to 108 nm. At even longer times, there was little further change in $A_{1000/525}$, but D_H grew to 498 nm within 1 min.

Strong SPR shifts into the NIR region have been observed in a variety of gold nanoclusters as a result of the overlap of hybridized plasmon modes.[49] The shifts are related to the interparticle spacings (<10% of the particle diameter), the nanocluster size, which governs the number of interparticle contacts, and the anisotropy in cluster shape.[26,28,31,49−51] As the size increases, the increase in the number of contacts ("hot spots") between primary particles, where the electromagnetic fields are enhanced, shifts the SPR to longer wavelengths. SPR peak shifts on the order of several 100 nm have been observed as even two particles touch.[49] Furthermore, broad NIR spectra have been observed from the sintering of two to three 5 nm Au NPs.[36] With a generalized multiparticle Mie solution and the T-matrix method, the shift in the SPR resonance for linear NP chains and the 2D and 3D nanoclusters was calculated as a function of the particle separation relative to the diameter, $H/2a$. For the smallest $H/2a$ of 0.025, the peak maximum shifted to ∼700 nm for a 4-mer chain and 800 nm for a 32-mer chain for 40 nm particles. In our case, this ratio would correspond to an H of only 0.125 nm. At the same ratio of 0.025, similar shifts were seen for 20 and 40 nm 1D chains and 3D clusters.[51] This distance is an order of magnitude below the value of 1.38 nm for the spacing between two particles coated with a monolayer of citrate. Thus, the relatively low NIR extinction for the small nanoclusters produced with NaCl suggests that the vdW attraction and weak bridging were insufficient to produce interparticle spacings below 0.125 nm.

Eventually, for extremely large clusters where the number of contacts becomes large after ∼5 s with 75 mM NaCl, the red shift was large with an $A_{1000/525}$ of 1.0 even with spacings greater than 0.125 nm. A similar result has been reported previously for 14 nm Au NP citrated clusters assembled with NaCl.[9] In contrast, smaller red shifts have been observed for more strongly binding thiols, namely, thioglycolic acid (TGA), cysteine, and glutathione.[9,52−54] Therefore, it appears that the relatively high $A_{1000/525}$ for citrate may indicate that it is somewhat mobile on the surface or leaves open Au patches that my approach each other more closely than 1.38 nm.

Although similar aggregation rates were observed for the −45 mV relative to the −34 mV primary citrate particles, the sizes and NIR absorbance of the samples will now be shown to be consistently smaller. For instance, at 30 s for 75 mM NaCl, the cluster D_H for the −34 mV sample reached 369 nm, as was also the case for the −45 mV particles (Table 2). Figure 3b compares the UV−vis−NIR absorbance curves for the two types of primary particles at 1 and 30 s. In both cases, a lower $A_{1000/525}$ ratio is observed for the −45 mV particle sample, consistent with a smaller number of "hot spots" or electric field enhancement for the smaller nanoclusters (Table S2).[26,37−39] Furthermore, TEM images of the −34 mV, 75 mM NaCl samples after 2 s show closely spaced distinct primary particles within the clusters (Figure 3c; Table S6, row 12). However, at high resolution, a very small degree of sintering was evident as shown in Table S6, row 13. By 30 s, sintering was more extensive as shown in Figure 3d and Table S6, row 14. However, the sintering did not cause the complete conversion of any pair of touching particles to a single particle, so the number of hot spots within the cluster did not decrease significantly. Interestingly, for only 50 mM NaCl at 120 s, minimal sintering and weak NIR absorbance were observed, indicating greater separations between particles with the stronger electrostatic repulsion.

Effect of $CaCl_2$ on NP Aggregation. For the experiments with Ca^{2+}, the appropriate concentrations were chosen by first determining the CCC. From visual observations, a $CaCl_2$ concentration of ∼1.5 mM induced immediate aggregation for 0.15 mg/mL Au, characteristic of the CCC. This CCC was similar to the reported value of 2.1 mM for $CaCl_2$ for 30 and 60 nm Ag spheres and was ∼100-fold smaller than for NaCl.[17,48] From theory, the calculated CCCs for the Derjaguin approximation in the limit as $\Psi_0 \rightarrow \infty$ are ∼100-fold smaller

DOI: 10.1021/acs.langmuir.5b03639
Langmuir 2016, 32, 1127−1138

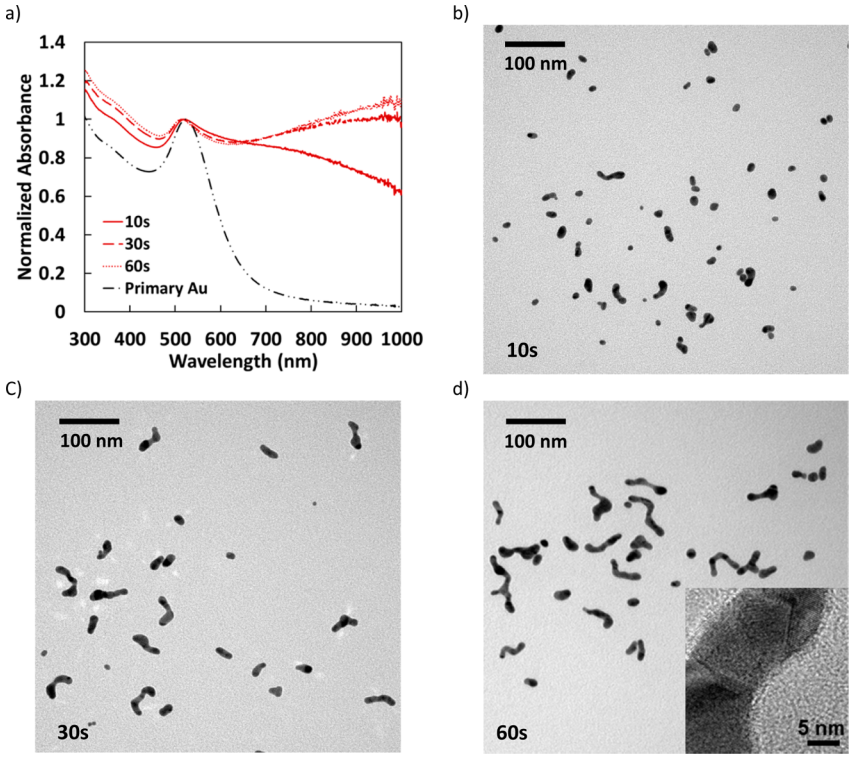

Figure 4. Absorbance vs wavelength at differing times for −34 mV initial particles and 0.22 mM $CaCl_2$. (b−d) TEM images at 10, 30, and 60 s. HR-TEM image of sintering of aggregates is shown in the inset of d.

for a 2:1 than for a 1:1 electrolyte.[55] Therefore, $CaCl_2$ may be used to form nanoclusters at much lower ionic strengths, whereby the longer Debye lengths may potentially be utilized to influence the morphology.

Notably different morphologies and NIR absorbance were observed for nanoclusters made in the presence of the much more dilute divalent Ca^{2+} relative to Na^+. Figure 4 shows the absorbance spectra and TEM images for assembled clusters made from −34 mV citrate primary particles in the presence of 0.22 mM $CaCl_2$ over 60 s. The $A_{1000/525}$ ratio rose quickly to 0.6 within 10 s and then increased to 1.1 at 60 s with an upward sloping curve suggesting the onset of a second, broad peak in the NIR around 1000 nm. TEM images in different time intervals show the assembly of what appears to be NP dimers and trimers forming into elongated, branched nanochains over 60 s (Figure 4b−d). At 10 s, a large number of dimers are present along with larger aggregates, with a TEM number-average size of 16.2 ± 8.8 nm (Table S7, row 1). Here, very few single primary particles are present.

Sintering was observed for Ca^{2+} in Figure 4 and Figure S3 (high-resolution TEM) and for Na^+ in the inset of Figure 3d and in Figure S3, despite the low temperature. The images for both $CaCl_2$ chains and NaCl aggregates show similar 0.24−0.26 nm lattice spacings for clusters made with either electrolyte, close to the 0.24 nm spacing characteristic of the (111) plane for Au.[56] Although elevated temperatures are typically used to produce sintering, many other studies have observed sintering at room temperature when two particles come into close contact, particularly for low ligand coverages.[6,36,40,57] The self-assembly of Au nanocrystals into 2D nanowire arrays was investigated for dodecanethiol-coated Ag nanocrystals.[57] For example, Ag nanowire arrays were formed only upon decreasing the dodecanethiol surface coverage to allow the particles to approach each other to within 0.5 nm to drive adhesion.[46] For higher dodecanethiol coverages where the spacing was 1.6 nm, coalescence was too weak for the formation of nanowires. Similarly, upon partial removal of TGA ligands, pearl necklaces of closely spaced CdTe NPs fused into a single nanowire crystal, with a diameter similar to that of the primary particles.[6] In another example, the degree of sintering of 17 nm citrate Au NPs was tuned by the amount of time used to desorb citrate ligands by dialysis.[40] The sintering was thought to occur only for "reactive collisions" that shared the same crystallographic planes at the interface. For citrate ligands, the much smaller spacing of 1.4 nm[35] compared to 3 nm for dodecanethiol would favor a closer approach. At these close spacings, it is conceivable that the reduction of any dissolved gold ions (or complexed Au ions) in solution by sodium citrate could contribute to the growth of the necks between primary particles.

Remarkably, $A_{1000/525}$ was already over 0.6 after only 10 s (Figure 4a), despite the very small size of the sintered oligomers (nanochains). After 30 s, the chains were elongated with an average length of 24.3 ± 14.3 nm and $A_{1000/525}$ of ∼1.0 as the formation of branches became visible. By 60 s, the chains were more branched and polydisperse with an $A_{1000/525}$ ratio of 1.1 and an average length of 30.5 ± 17.2 nm, as shown in Figure 4d and Table S7, row 3. These results indicate that the overlap of the plasmon modes even for small, sintered, oligomeric chains is sufficient to produce broad, high-NIR absorbance. This result is not surprising in view of the aforementioned large shift for particles that touch[49] and the high degree of asymmetry in shape for the branched nanochains. However, because of the polydispersity in shape and degrees of sintering at the particle interfaces, the peak is quite broad as opposed to the narrow secondary, longitudinal peaks characteristic of cylindrical nanorods.[58] Furthermore, the NIR absorbance was much greater than with NaCl for the

DOI: 10.1021/acs.langmuir.5b03639
Langmuir 2016, 32, 1127−1138

small, much less sintered nanoclusters. For $CaCl_2$, the closer interparticle spacings and consequently greater sintering between primary particles, relative to NaCl, given the stronger bridging attraction shown in Figure 2, produced the much greater NIR absorbance.

Beyond 60 s, the length of the branched nanochain structures increased up to ~100 nm within 1800 s (Figure 5a). A decrease in the non-normalized UV−vis−NIR absorbance of the sample indicated that the additional growth resulted in slight precipitation from either the formation of a small population of much larger aggregates present in the solution or the aggregation of preformed clusters in solution (Figure S2).

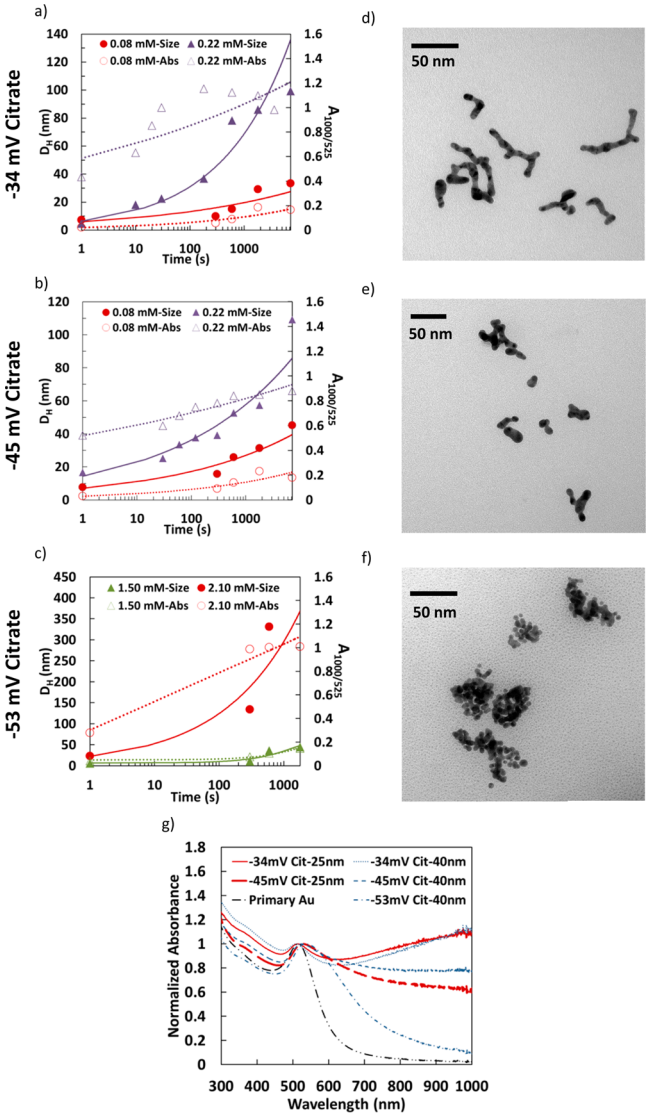

Figure 5. (a−c) Effect of $CaCl_2$ concentration and initial particle zeta potential on UV−vis−NIR absorbance and D_H of nanoclusters vs time. TEM images of an ~40 nm representative sample are shown for (d) −34 mV primary particles and 0.22 mM $CaCl_2$ at 120 s, (e) −45 mV primary particles and 0.22 mM $CaCl_2$ at 120 s, and (f) −53 mV primary particles and 1.5 mM $CaCl_2$ at 3600 s. (g) Normalized absorbance for 25 and 40 nm clusters formed with 0.22 mM $CaCl_2$ for −34 and −45 mV particles and 1.50 mM $CaCl_2$ for −53 mV particles. The 25 nm clusters were made at 30 s. The 40 nm clusters were made after 180 s for both the −34 and −45 mV particles and after 600 s for the −53 mV particles.

However, samples made within 300 s were stable for over 20 days at room temperature as characterized by UV−vis−NIR absorbance and D_H in Table S3 and Figure S2e,f.

In contrast to the results for 0.22 mM $CaCl_2$, much smaller particles were formed for −34 mV Au with only 0.08 mM $CaCl_2$. With the more negative ζ of −20.9 ± 3.3 mV, the size increased to only 14 nm within the first 300 s, with very little change in the NIR absorbance. With the greater electrostatic repulsion and weaker bridging attraction with the lower Ca^{2+} concentration, the aggregates did not grow significantly or undergo significant sintering even up to 1800 s (Table S6, rows 1 and 2). Thus, it appears that a higher driving force for aggregation with 0.22 mM $CaCl_2$ is needed to produce the small spacings and subsequent sintering that give high NIR absorbance.

For the more highly charged −45 mV primary particles (Figure 5b,e), the results will now be shown to be similar to those observed at −34 mV, but with smaller sizes at early times and significantly weaker NIR absorbance. Minimal aggregation was again observed with 0.08 mM $CaCl_2$. The clusters grew to only 16 nm aggregates with an $A_{1000/525}$ of 0.1 in 60 s. Again, as the concentration of Ca^{2+} was increased to 0.22 mM, the greater electrostatic screening and bridging attraction resulted in a significantly higher NIR absorbance, even for very small branched chains. After 1 s, the size grew to 20 nm with an $A_{1000/525}$ of 0.5 and further to 33 nm with an $A_{1000/525}$ of 0.7 by 60 s. Interestingly, the D_H values were similar for the −45 and −34 mV primary particle aggregates under the same conditions up to 180 s. At longer times, the less highly charged cluster aggregates grew more rapidly. At 1800 s, the D_H was 86 nm with an $A_{1000/525}$ of 1.1 for the −34 mV primary particles and 57 nm with an $A_{1000/525}$ of 0.9 for the −45 mV chains. For an even higher $CaCl_2$ concentration of 0.5 mM, the nanochain grew rapidly with a D_H of 229 nm after 300 s, and the particles precipitated and settled within 600 s. Despite the lower degree of growth and NIR absorbance for the more highly charged −45 mV samples, branched-chain morphologies were observed in both cases as shown in Figure 5e and Table S6, row 9.

To rule out any potential changes in morphology from halide ion complexation and etching of Au, clusters were made using 0.22 mM $Ca(NO_3)_2$.[59] Despite a 10 nm larger average D_H for the nitrate salt, the NIR extinction and linear branched-chain morphology were present for both samples, as seen in Figure S4. Thus, it is unlikely that Cl^- etching played a significant role in the nanochain formation or sintering relative to NO_3^-.

Although partially sintered branched chains were observed for the −45 and −34 mV primary particles, sintering was not observed during the assembly of the −53 mV primary particles with 3 mM sodium citrate (Figure 5c). After 3600 s, the solution remained red and dimer and trimers were formed with a D_H of 17 nm (Table S2). When the concentration of $CaCl_2$ was increased to 1.5 mM, the particles grew to 48 nm within 3600 s, but $A_{1000/525}$ was only 0.19 (Figure 5c). The morphology of the resulting clusters resembled the spherical aggregates observed in the presence of NaCl, with notable interparticle spacings (Figure 5f). In the presence of excess citrate ions, multilayers of citrate can form on Au particle surfaces through H bonding.[35] The greater steric repulsion for the higher citrate coverage resulted in a more spherical geometry, as expected with only partial capping of the Au surfaces. Despite the high concentration of bridging Ca^{2+} cations, the greater spacing with the longer-ranged steric repulsion prevented the NIR $A_{1000/525}$ values from reaching 1.0

DOI: 10.1021/acs.langmuir.5b03639
Langmuir 2016, 32, 1127−1138

until the D_H was over 100 nm (in the case of 2.1 mM $CaCl_2$ concentrations). Given the larger interparticle spacings and lack of sintering, larger numbers of hot spots between individual particles were required to produce a high NIR absorbance for these particles, relative to the case of the −45 and −34 mV primary particles.[26,49]

In Figure 5g, the spectra are shown for samples sorted by the primary particle charge and the nanocluster size after assembly. These experiments all used $CaCl_2$ but with different times and concentrations to achieve the desired cluster size. The NIR absorbance increased as the primary particle charge was reduced, but it changed very little as D_H increased from 25 to 40 nm. For ∼25 nm clusters, $A_{1000/525}$ was 0.65 for −45 mV primary NPs and 1.10 for −34 mV NPs. Similarly, for ∼40 nm nanoclusters, $A_{1000/525}$ decreased with the primary NP charge from 1.10 (−34 mV) to 0.75 (−45 mV) and finally to 0.10 (−53 mV). Given the very small particle spacings of <0.5 nm along with the sintering, it was not possible to discern the difference in particle spacing for the −34 and −45 mV cases by TEM (Figure 5d,e and Table S6, rows 1−9). However, as the electrostatic repulsion increases, expected larger spacings between primary particles and a decrease in sintering would result in weaker NIR absorbance, as observed.

Another way to relate the spectra to morphology is to determine what D_H is needed to produce a given $A_{1000/525}$ as a function of the primary particle charge and electrolyte type (Table 3). At an $A_{1000/525}$ of 0.6, a D_H below 70 nm could be achieved for three of the four conditions. At each $A_{1000/525}$, the strong bridging attraction from Ca^{2+} compared to that from Na^+ resulted in a much smaller D_H. This difference in D_H is accentuated as $A_{1000/525}$ increases. For an $A_{1000/525}$ of 0.9, D_H values for clusters made with $CaCl_2$ were 21 and 41 nm for −34 and −45 mV primary NPs, respectively, whereas much greater values were required for those formed with NaCl. It was not possible to achieve an $A_{1000/525}$ of 1.0 with the more highly charged −45 mV particles, whereas it could be attained for a D_H of only 33 nm in the −34 mV case with $CaCl_2$. These differences emphasize the strong correlation between interparticle spacing and sintering with the NIR extinction. The small interparticle spacings and asymmetry in shape with sintering for the branched nanochains produce high NIR absorbance with many fewer hot spots and much smaller D_H values than for the more spherical, loosely packed NaCl aggregates in Figure 3c and in a previous study.[9] Even when sintering occurred for the NaCl clusters, a more rounded, spherical geometry led to high NIR only with large sizes, as seen in Figure 3.

Table 3. D_H Values and Reaction Times for Clusters Made with Either −34 or −45 mV Primary Particles and Electrolytes to Achieve a Given $A_{1000/525}$ Ratio

		$A_{1000/525}$					
		0.6		0.8		1.0	
primary particle	salt conc (mM)	time (s)	D_H (nm)	time (s)	D_H (nm)	time (s)	D_H (nm)
−34 mV	0.22 mM $CaCl_2$	10	18.0	20	21.0	30	32.7
	75 mM NaCl	3	66.7	5	108	30	369
−45 mV	0.22 mM $CaCl_2$	30	25.0	300	41.0		
	75 mM NaCl	5	141	20	172		

Mechanism for the Formation of Branched Chains. A mechanism for the formation of the branched chains may be developed by considering the effects of the various interactions in Figure 2, including bridging attraction. The formation of linear chains has been widely attributed to dipole−dipole interactions, for example, in the case of CdTe semiconductor NPs with a permanent dipole.[6] Linear 1D assemblies were observed primarily in the presence of Ca^{2+} cations for the −45 and −34 mV primary citrate NPs but not for NaCl or the −53 mV primary NPs. For Au particles where the conductive cores do not have a permanent dipole moment, the dipole moment may be generated from inhomogeneities in the surface ligands, for example, for mixtures of charged and uncharged ligands such as citrate and 2-mecaptothanol.[50] For Au NPs capped with TGA, the Au−S bonds were thought to produce dipoles that led to 1D assembly.[36] Alternatively, the oriented interactions between glutamic acid dipoles on Au NP surfaces oriented the particles into linear chains.[60] In our case, dipole moments may be produced by inhomogeneities in the packing of the citrate ligands on the particle surfaces. In a study with FTIR and X-ray photoelectron spectroscopy, hydrogen bonds between citrate molecules led to the formation of citrate networks on the surface, when the citrate coverage was 45%.[35] In our case, these inhomogeneities may be further enhanced by interparticle bridging of citrate with the Ca^{2+} ions.[17,48] With the higher citrate coverage for the −53 mV particles, the lack of 1D chain formation may suggest that the dipole moment decreased as citrate became more uniform on the surface.

Zhang et al. demonstrate that the length of nonfused 14 nm gold nanoparticle chains could be controlled via the addition of NaCl to modulate electrostatic repulsion relative to the vdW and dipolar attraction between primary particles.[9] When the electrostatic repulsion was at least 2 -fold greater than the vdW force, chains were formed, given weaker electrostatic repulsion at the chain ends than on the sides. In contrast, when electrostatic repulsion was weaker than the vdW attraction, the addition of particles was no longer selective toward chain ends and 3D assemblies were formed. Following this model, as a particle approaches a growing chain, we assume that the balance between electrostatic repulsion and vdW attraction would favor the chain ends for Ca^{2+} because $V_{elect} > V_{vdW}$ for the values shown in Figure 2. At particle separations greater than ∼3 nm, the bridging interaction is weak. The much lower concentration of Ca^{2+} needed to form nanochains relative to that for Na^+ for cluster formation led to thicker diffuse counterion layers and greater electrostatic repulsion, which are conditions needed to direct 1D assembly as observed.

This model may be modified to include the role of the bridging attraction that becomes strong at very close separations (Figure 2b). Our results indicate that despite the large strength of this bridging attraction, the greater electrostatic repulsion at chain ends for thick double layers with Ca^{2+} favored chains relative to Na^+ (Figure 2a). Thus, the potential at larger separations before bridging becomes strong thus appearing to guide the direction of approach of the primary particles. Here, a 1D cluster is formed by strong electrostatic repulsion from the very thick double layer, weak vdW attraction, and the strong bridging attraction at very short range in the presence of the attraction between the dipoles on the particles. These forces may be manipulated by changing the cation concentration and valence to influence the double-layer

DOI: 10.1021/acs.langmuir.5b03639
Langmuir 2016, 32, 1127−1138

thickness and the bridging attraction to control the nanocluster morphology. Furthermore, the interparticle Ca^{2+} bridging attraction provided a strong attractive driving force to overcome the strong electrostatic repulsion, despite the very low Ca^{2+} concentration. Therefore, both attraction and repulsion were relatively strong, yet the balance between these two interactions could be tuned with the Ca^{2+} concentration in order to control the cluster morphology.

CONCLUSIONS

The size and morphology of nanoclusters of small 5 nm citrate-coated Au primary particles were controlled by tuning the electrostatic repulsion and bridging attraction in the presence of vdW and dipolar attraction. In the case of Ca^{2+}, strong interparticle bridging with adsorbed citrate anions produced branched nanochains in <60 s with closely spaced and sintered primary particles, resulting in a broad NIR extinction peak out to 1100 nm. This high level of NIR extinction, produced by the sintered branched nanochains, is unusual for such small nanochains with lengths as short as 20 nm. The branched nanochains were formed by strong electrostatic repulsion with a very thick double layer to favor nanoparticle addition on the chain ends instead of the sides, relative to weaker vdW forces.[9] At very close spacings on the order of 1.4 nm or less, the particles were bound to the cluster by strong short-ranged bridging attraction in addition to vdW attraction. In contrast, spherical nanoclusters were formed with NaCl, often with distinct spacings between the primary particles and minimal sintering according to TEM, resulting in weak NIR extinction. For Na^{+}, much higher ionic strengths were needed to screen the electrostatic repulsion, and the bridging driving force was much weaker. Consequently, thinner double layers and weaker electrostatic repulsion no longer favored anisotropic particle growth and sintering into chains. For Ca^{2+}, interparticle bridging of citrate may have produced dipoles on the particle surfaces that are known to favor anisotropy. In each case, the aggregation of the nanoclusters and nanochains was quenched simply by dilution to lower the ionic strength to increase the electrostatic repulsion and weaken the interparticle bridging. The resulting particles were stable over 20 days. For a desired nanocluster size of less than 50 nm, the small 5 nm primary particles provided a larger number of hot spots for electrical field enhancement, resulting in larger NIR shifts relative to those for much more commonly studied particles larger than 10 nm. The ability to design the size and shape of nanoclusters, as well as the interparticle spacings by tuning bridging and electrostatic interactions, may be expected to be quite general and of broad applicability in materials synthesis.

ASSOCIATED CONTENT

Supporting Information

The Supporting Information is available free of charge on the ACS Publications website at DOI: 10.1021/acs.langmuir.5b03639.

Summary tables of all samples presented in the main text and additional DLS, UV−vis−NIR, and TEM data for primary particles, nanoclusters, and nanochains are found in this document (PDF)

AUTHOR INFORMATION

Corresponding Author

*E-mail: kpj@che.utexas.edu.

Author Contributions

R.J.S. and E.M. contributed equally to this article.

Notes

The authors declare no competing financial interest.

ACKNOWLEDGMENTS

K.P.J. acknowledges support from NSF (CBET-0968038) and NIH (CA143663). K.P.J. and T.M.T acknowledge support from the Welch Foundation (F-1319 and F-1696, respectively) and NSF (CBET-1247945).

REFERENCES

(1) Hill, L. J.; Pinna, N.; Char, K.; Pyun, J. Colloidal polymers from inorganic nanoparticle monomers. *Prog. Polym. Sci.* **2015**, *40*, 85−120.
(2) Klinkova, A.; Choueiri, R. M.; Kumacheva, E. Self-assembled plasmonic nanostructures. *Chem. Soc. Rev.* **2014**, *43* (11), 3976−3991.
(3) Lu, Z.; Yin, Y. Colloidal nanoparticle clusters: functional materials by design. *Chem. Soc. Rev.* **2012**, *41*, 6874−6887.
(4) Romo-Herrera, J. M.; Alvarez-Puebla, R. A.; Liz-Marzan, L. M. Controlled assembly of plasmonic colloidal nanoparticle clusters. *Nanoscale* **2011**, *3* (4), 1304−1315.
(5) Wang, T.; LaMontagne, D.; Lynch, J.; Zhuang, J.; Cao, Y. C. Colloidal superparticles from nanoparticle assembly. *Chem. Soc. Rev.* **2013**, *42* (7), 2804−2823.
(6) Tang, Z.; Kotov, N. A.; Giersig, M. Spontaneous organization of single CdTe nanoparticles into luminescent nanowires. *Science* **2002**, *297* (5579), 237−240.
(7) Sinyagin, A. Y.; Belov, A.; Tang, Z.; Kotov, N. A. Monte Carlo computer simulation of chain formation from nanoparticles. *J. Phys. Chem. B* **2006**, *110* (14), 7500−7507.
(8) Li, M.; Johnson, S.; Guo, H.; Dujardin, E.; Mann, S. A Generalized Mechanism for Ligand-Induced Dipolar Assembly of Plasmonic Gold Nanoparticle Chain Networks. *Adv. Funct. Mater.* **2011**, *21* (5), 851−859.
(9) Zhang, H.; Wang, D. Controlling the Growth of Charged-Nanoparticle Chains through Interparticle Electrostatic Repulsion. *Angew. Chem.* **2008**, *120* (21), 4048−4051.
(10) Enustun, B. V.; Turkevich, J. Coagulation of Colloidal Gold. *J. Am. Chem. Soc.* **1963**, *85* (21), 3317−3328.
(11) Han, X.; Goebl, J.; Lu, Z.; Yin, Y. Role of Salt in the Spontaneous Assembly of Charged Gold Nanoparticles in Ethanol. *Langmuir* **2011**, *27*, 5282−5289.
(12) Burns, C.; Spendel, W.; Puckett, S.; Pacey, G. Solution ionic strength effect on gold nanoparticle solution color transition. *Talanta* **2006**, *69* (4), 873−876.
(13) Elimelech, M.; Gregory, J.; Jia, X. *Particle Deposition and Aggregation: Measurement, Modelling and Simulation*; Butterworth-Heinemann: Oxford, England, 1998.
(14) Hiemenz, P. C.; Rajagopalan, R. *Principles of Colloid and Surface Chemistry*; CRC Press: Boca Raton, FL, 1997; Vol. *14*.
(15) Wang, D.; Tejerina, B.; Lagzi, I.; Kowalczyk, B.; Grzybowski, B. A. Bridging interactions and selective nanoparticle aggregation mediated by monovalent cations. *ACS Nano* **2011**, *5* (1), 530−536.
(16) Yao, Q.; Luo, Z.; Yuan, X.; Yu, Y.; Zhang, C.; Xie, J.; Lee, J. Y. Assembly of nanoions via electrostatic interactions: ion-like behavior of charged noble metal nanoclusters. *Sci. Rep.* **2014**, *4*.10.1038/srep03848
(17) Huynh, K. A.; Chen, K. L. Aggregation kinetics of citrate and polyvinylpyrrolidone coated silver nanoparticles in monovalent and divalent electrolyte solutions. *Environ. Sci. Technol.* **2011**, *45* (13), 5564−5571.
(18) Berchmans, S.; Thomas, P. J.; Rao, C. Novel effects of metal ion chelation on the properties of lipoic acid-capped Ag and Au nanoparticles. *J. Phys. Chem. B* **2002**, *106* (18), 4647−4651.
(19) Sokolov, K.; Stover, R.; Joshi, P.; Yoon, S. J.; Murthy, A.; Emelianov, S.; Johnston, K. *Biodegradable Plasmonic Nanoparticles: Overcoming Clinical Translation Barriers*; Optical Molecular Probes,

DOI: 10.1021/acs.langmuir.5b03639
Langmuir 2016, 32, 1127−1138

Imaging and Drug Delivery, 2015; Optical Society of America, p OM3D.4.
(20) Yoon, S. J.; Mallidi, S.; Tam, J. M.; Tam, J. O.; Murthy, A.; Johnston, K. P.; Sokolov, K. V.; Emelianov, S. Y. Utility of biodegradable plasmonic nanoclusters in photoacoustic imaging. *Opt. Lett.* **2010**, *35* (22), 3751−3753.
(21) Hashmi, A. S. K. Gold-catalyzed organic reactions. *Chem. Rev.* **2007**, *107* (7), 3180−3211.
(22) Huang, D.; Liao, F.; Molesa, S.; Redinger, D.; Subramanian, V. Plastic-compatible low resistance printable gold nanoparticle conductors for flexible electronics. *J. Electrochem. Soc.* **2003**, *150* (7), G412−G417.
(23) Chithrani, B. D.; Stewart, J.; Allen, C.; Jaffray, D. A. Intracellular uptake, transport, and processing of nanostructures in cancer cells. *Nanomedicine* **2009**, *5* (2), 118−127.
(24) Mallidi, S.; Larson, T.; Tam, J.; Joshi, P. P.; Karplouk, A.; Sokolov, K.; Emelianov, S. Multiwavelength Photoacoustic Imaging and Plasmon Resonance Coupling of Gold Nanoparticles for Selective Detection of Cancer. *Nano Lett.* **2009**, *9* (8), 2825−2831.
(25) Weissleder, R. A clearer vision for in vivo imaging. *Nat. Biotechnol.* **2001**, *19*, 316−317.
(26) Khlebtsov, B.; Zharov, V.; Melnikov, A.; Tuchin, V.; Khlebtsov, N. Optical amplification of photothermal therapy with gold nanoparticles and nanoclusters. *Nanotechnology* **2006**, *17*, 5167−5179.
(27) Khlebtsov, N.; Dykman, L.; Krasnov, Y. M.; Mel'nikov, A. Light absorption by the clusters of colloidal gold and silver particles formed during slow and fast aggregation. *Colloid J.* **2000**, *62* (6), 765−779.
(28) Lassiter, J. B.; Aizpurua, J.; Hernandez, L. I.; Brandl, D. W.; Romero, I.; Lal, S.; Hafner, J. H.; Nordlander, P.; Halas, N. J. Close encounters between two nanoshells. *Nano Lett.* **2008**, *8* (4), 1212−1218.
(29) Polavarapu, L.; Perez-Juste, J.; Xu, Q.-H.; Liz-Marzan, L. M. Optical sensing of biological, chemical and ionic species through aggregation of plasmonic nanoparticles. *J. Mater. Chem. C* **2014**, *2* (36), 7460−7476.
(30) Srivastava, S.; Frankamp, B. L.; Rotello, V. M. Controlled Plasmon Resonance of Gold Nanoparticles Self-Assembled with PAMAM Dendrimers. *Chem. Mater.* **2005**, *17* (3), 487−490.
(31) Khlebtsov, B. N.; Khanadeyev, V. A.; Ye, J.; Mackowski, D. W.; Borghs, G.; Khlebtsov, N. G. Coupled plasmon resonances in monolayers of metal nanoparticles and nanoshells. *Phys. Rev. B: Condens. Matter Mater. Phys.* **2008**, *77* (3), 035440.
(32) Lim, I. I. S.; Ip, W.; Crew, E.; Njoki, P. N.; Mott, D.; Zhong, C.-J.; Pan, Y.; Zhou, S. Homocysteine-Mediated Reactivity and Assembly of Gold Nanoparticles. *Langmuir* **2007**, *23* (2), 826−833.
(33) Wang, M.-H.; Li, Y.-J.; Xie, Z.-X.; Liu, C.; Yeung, E. S. Fabrication of large-scale one-dimensional Au nanochain and nanowire networks by interfacial self-assembly. *Mater. Chem. Phys.* **2010**, *119* (1), 153−157.
(34) Polavarapu, L.; Xu, Q.-H. A single-step synthesis of gold nanochains using an amino acid as a capping agent and characterization of their optical properties. *Nanotechnology* **2008**, *19* (7), 075601.
(35) Park, J.-W.; Shumaker-Parry, J. S. Structural study of citrate layers on gold nanoparticles: role of intermolecular interactions in stabilizing nanoparticles. *J. Am. Chem. Soc.* **2014**, *136* (5), 1907−1921.
(36) Lee, J.; Zhou, H.; Lee, J. Small molecule induced self-assembly of Au nanoparticles. *J. Mater. Chem.* **2011**, *21* (42), 16935−16942.
(37) Murthy, A. K.; Stover, R. J.; Borwankar, A. U.; Nie, G. D.; Gourisankar, S.; Truskett, T. M.; Sokolov, K. V.; Johnston, K. P. Equilibrium Gold Nanoclusters Quenched with Biodegradable Polymers. *ACS Nano* **2013**, *7* (1), 239−251.
(38) Stover, R. J.; Murthy, A. K.; Nie, G. D.; Gourisankar, S.; Dear, B. J.; Truskett, T. M.; Sokolov, K. V.; Johnston, K. P. Quenched Assembly of NIR-Active Gold Nanoclusters Capped with Strongly Bound Ligands by Tuning Particle Charge via pH and Salinity. *J. Phys. Chem. C* **2014**, *118* (26), 14291−14298.
(39) Tam, J. M.; Murthy, A. K.; Ingram, D. R.; Nguyen, R.; Sokolov, K. V.; Johnston, K. P. Kinetic Assembly of Near-IR Active Gold Nanoclusters Using Weakly Adsorbing Polymers to Control the Size. *Langmuir* **2010**, *26* (11), 8988−8999.
(40) Dutta, A.; Das, S.; Paul, A.; Chattopadhyay, A. Kinetics of reaction of gold nanoparticles following partial removal of stabilizers. *J. Nanopart. Res.* **2015**, *17* (6), 1−13.
(41) Grouchko, M.; Popov, I.; Uvarov, V.; Magdassi, S.; Kamyshny, A. Coalescence of silver nanoparticles at room temperature: unusual crystal structure transformation and dendrite formation induced by self-assembly. *Langmuir* **2009**, *25* (4), 2501−2503.
(42) Grabar, K. C.; Allison, K. J.; Baker, B. E.; Bright, R. M.; Brown, K. R.; Freeman, R. G.; Fox, A. P.; Keating, C. D.; Musick, M. D.; Natan, M. J. Two-Dimensional Arrays of Colloidal Gold Particles: A Flexible Approach to Macroscopic Metal Surfaces. *Langmuir* **1996**, *12* (10), 2353−2361.
(43) Khlebtsov, B. N.; Khlebtsov, N. G. On the measurement of gold nanoparticle sizes by the dynamic light scattering method. *Colloid J.* **2011**, *73* (1), 118−127.
(44) Grabar, K. C.; Freeman, R. G.; Hommer, M. B.; Natan, M. J. Preparation and Characterization of Au Colloid Monolayers. *Anal. Chem.* **1995**, *67* (4), 735−743.
(45) Murthy, A. K.; Stover, R. J.; Hardin, W. G.; Schramm, R.; Nie, G. D.; Gourisankar, S.; Truskett, T. M.; Sokolov, K. V.; Johnston, K. P. Charged Gold Nanoparticles with Essentially Zero Serum Protein Adsorption in Undiluted Fetal Bovine Serum. *J. Am. Chem. Soc.* **2013**, *135*, 7799−7802.
(46) Israelachvili, J. N. *Intermolecular and Surface Forces*, 3rd ed.; Elsevier: New York, 2011.
(47) Walser, M. Dissociation constants for complexes of citrate with sodium, potassium, calcium, and magnesium ions. *J. Phys. Chem.* **1961**, *65* (1), 159−161.
(48) Baalousha, M.; Nur, Y.; Römer, I.; Tejamaya, M.; Lead, J. R. Effect of monovalent and divalent cations, anions and fulvic acid on aggregation of citrate-coated silver nanoparticles. *Sci. Total Environ.* **2013**, *454*−*455*, 119−131.
(49) Halas, N. J.; Lal, S.; Chang, W.-S.; Link, S.; Nordlander, P. Plasmons in Strongly Coupled Metallic Nanostructures. *Chem. Rev.* **2011**, *111*, 3913−3961.
(50) Lin, S.; Li, M.; Dujardin, E.; Girard, C.; Mann, S. One-Dimensional Plasmon Coupling by Facile Self-Assembly of Gold Nanoparticles into Branched Chain Networks. *Adv. Mater.* **2005**, *17* (21), 2553−2559.
(51) Esteban, R.; Taylor, R. W.; Baumberg, J. J.; Aizpurua, J. How chain plasmons govern the optical response in strongly interacting self-assembled metallic clusters of nanoparticles. *Langmuir* **2012**, *28* (24), 8881−8890.
(52) Zhang, H.; Fung, K.-H.; Hartmann, J. r.; Chan, C.; Wang, D. Controlled chainlike agglomeration of charged gold nanoparticles via a deliberate interaction balance. *J. Phys. Chem. C* **2008**, *112* (43), 16830−16839.
(53) Mandal, S.; Gole, A.; Lala, N.; Gonnade, R.; Ganvir, V.; Sastry, M. Studies on the reversible aggregation of cysteine-capped colloidal silver particles interconnected via hydrogen bonds. *Langmuir* **2001**, *17* (20), 6262−6268.
(54) Fu, R.; Li, J.; Yang, W. Aggregation of glutathione-functionalized Au nanoparticles induced by Ni2+ ions. *J. Nanopart. Res.* **2012**, *14* (6), 1−8.
(55) Hsu, J.-P.; Kuo, Y.-C. The critical coagulation concentration of counterions: Spherical particles in asymmetric electrolyte solutions. *J. Colloid Interface Sci.* **1997**, *185* (2), 530−537.
(56) Wang, Y.; Liang, W.; Geng, C. Coalescence behavior of gold nanoparticles. *Nanoscale Res. Lett.* **2009**, *4* (7), 684−688.
(57) Korgel, B. A.; Fitzmaurice, D. Self-assembly of silver nanocrystals into two-dimensional nanowire arrays. *Adv. Mater.* **1998**, *10* (9), 661−665.
(58) Pérez-Juste, J.; Pastoriza-Santos, I.; Liz-Marzán, L. M.; Mulvaney, P. Gold nanorods: synthesis, characterization and applications. *Coord. Chem. Rev.* **2005**, *249* (17), 1870−1901.
(59) Kedia, A.; Kumar, P. S. Halide ion induced tuning and self-organization of gold nanostars. *RSC Adv.* **2014**, *4* (9), 4782−4790.

DOI: 10.1021/acs.langmuir.5b03639
Langmuir 2016, 32, 1127−1138

(60) Liu, Y.; Qiao, L.; Liu, L.; Guo, R. pH Controlled assembly of gold nanoparticles coated with glutamic acid: Assembly mechanism, the effect of NaBr, and SERS performance. *Colloids Surf., A* **2015**, *474*, 92−100.

DOI: 10.1021/acs.langmuir.5b03639
Langmuir 2016, 32, 1127−1138